Monthly Notices
of the
ROYAL ASTRONOMICAL SOCIETY

MNRAS **493,** 4830–4844 (2020)
Advance Access publication 2020 February 28

doi:10.1093/mnras/staa592

Cross-correlating *Planck* with VST ATLAS LRGs: a new test for the ISW effect in the Southern hemisphere

Behzad Ansarinejad [1]★, Ruari Mackenzie [2]★, Tom Shanks [1]★ and Nigel Metcalfe [1]

[1] *Department of Physics, Durham University, South Road, Durham DH1 3LE, UK*
[2] *Department of Physics, ETH Zürich, Wolfgang-Pauli-Strasse 27, CH-8093 Zürich, Switzerland*

Accepted 2020 February 25. Received 2020 February 11; in original form 2019 September 25

ABSTRACT

The integrated Sachs–Wolfe (ISW) effect probes the late-time expansion history of the Universe, offering direct constraints on dark energy. Here, we present our measurements of the ISW signal at redshifts of $\bar{z} = 0.35$, 0.55, and 0.68, using the cross-correlation of the *Planck* cosmic microwave background temperature map with ∼0.5 million luminous red galaxies (LRGs) selected from the VST ATLAS survey. We then combine these with previous measurements based on WMAP and similar SDSS LRG samples, providing a total sample of ∼2.1 million LRGs covering ∼12 000 deg^2 of sky. At $\bar{z} = 0.35$ and $\bar{z} = 0.55$, we detect the ISW signal at 1.2σ and 2.3σ (or 2.6σ combined), in agreement with the predictions of lambda cold dark matter (ΛCDM). We verify these results by repeating the measurements using the BOSS LOWZ and CMASS, spectroscopically confirmed LRG samples. We also detect the ISW effect in three magnitude limited ATLAS + SDSS galaxy samples extending to $z \approx 0.4$ at $\sim 2\sigma$ per sample. However, we do not detect the ISW signal at $\bar{z} = 0.68$ when combining the ATLAS and SDSS results. Further tests using spectroscopically confirmed eBOSS LRGs at this redshift remain inconclusive due to the current low sky coverage of the survey. If the ISW signal is shown to be redshift dependent in a manner inconsistent with the predictions of ΛCDM, it could open the door to alternative theories such as modified gravity. It is therefore important to repeat the high-redshift ISW measurement using the completed eBOSS sample, as well as deeper upcoming surveys such as DESI and LSST.

Key words: cosmology: cosmic background radiation – observations – dark energy – large-scale structure of Universe.

1 INTRODUCTION

Based on the latest observational evidence, the Universe is believed to be spatially flat (Planck Collaboration XIII 2016b) and undergoing a late-time accelerating state of expansion (Riess et al. 1998; Alam et al. 2017). In the current standard model of cosmology lambda cold dark matter (ΛCDM), dark energy, parametrized as a cosmological constant (Λ), is believed to be the driving force behind this late-time accelerating expansion. Various alternatives to the cosmological constant have been proposed including modified gravity (Clifton et al. 2012), scale invariant (Maeder 2017), or spatially inhomogeneous cosmological models (see e.g. Dunsby et al. 2010; Rácz et al. 2017). As a consequence of the accelerated expansion of the Universe, cosmic microwave background (CMB) photons passing through gravitational potential wells, caused by large-scale structure such as galaxy clusters, are left with a net gain of energy as the potential wells become shallower as the photons cross them. The opposite effect takes place as the photons pass through gravitational potential peaks (i.e. voids) with the photons undergoing a net loss of energy. The combination of these phenomena leads to secondary anisotropies on the CMB temperature map known as the (late-time) integrated Sachs–Wolfe (ISW; Sachs & Wolfe 1967) effect. The signature of the ISW effect can be observed as a non-zero signal in the cross-correlation between the distribution of foreground tracers of mass (such as galaxies) and the temperature of CMB, providing a direct probe of the late-time expansion of the Universe.

Early attempts at measuring the ISW signal using the cross-correlation method, include an analysis of the *COBE* CMB map by Boughn & Crittenden (2002) followed by detections of the signal using the WMAP CMB data, albeit often at relatively low to moderate levels of significance (Scranton et al. 2003; Boughn & Crittenden 2004; Nolta et al. 2004; Corasaniti, Giannantonio & Melchiorri 2005; Padmanabhan et al. 2005; Cabré et al. 2006; Giannantonio et al. 2006; Rassat et al. 2007; Raccanelli et al. 2008; Granett, Neyrinck & Szapudi 2009; Bielby et al. 2010; Sawangwit et al. 2010; Kovács et al. 2013). Other studies have however claimed detections in the range of 3σ–5σ (Fosalba, Gaztañaga &

★ E-mail: behzad.ansarinejad@durham.ac.uk (BA); mruari@phys.ethz.ch (RM); tom.shanks@durham.ac.uk (TS)

© 2020 The Author(s)
Published by Oxford University Press on behalf of the Royal Astronomical Society

Downloaded from https://academic.oup.com/mnras/article-abstract/493/4/4830/5766327 by University of Durham user on 20 March 2020

Castander 2003; Fosalba & Gaztañaga 2004; McEwen et al. 2006; Vielva, Martínez-González & Tucci 2006; Giannantonio et al. 2008; Granett, Neyrinck & Szapudi 2008; Ho et al. 2008; Giannantonio et al. 2012; Goto, Szapudi & Granett 2012; Planck Collaboration XXI 2016c).

Another common approach in measuring the ISW signal is by stacking of voids and superclusters. Similar to the cross-correlation method, studies using this approach have obtained detection significances ranging from low to moderate (Granett, Kovács & Hawken 2015; Kovács et al. 2017), to 3σ or higher (Pápai, Szapudi & Granett 2011; Nadathur & Crittenden 2016; Planck Collaboration XXI 2016c; Cai et al. 2017). Interestingly, a number of these studies have reported a signal with a higher amplitude than expected based on ΛCDM predictions.

Here, we follow the work of Sawangwit et al. (2010) where the ISW analysis was performed on photometrically selected luminous red galaxies (LRGs) from SDSS in the Northern hemisphere. Three redshift-limited LRG samples were created allowing the measurement the ISW signal at redshifts of $\bar{z} = 0.35$, 0.55, and 0.68. Although an ISW signal consistent with ΛCDM was detected at $\bar{z} = 0.35$ and 0.55, no such signal was detected at $\bar{z} = 0.68$ albeit, as in the other two cases, the errors were significant. Given the implications of any ISW deviations from ΛCDM predictions, the lack of detection of the ISW signal at $\bar{z} = 0.68$ in SDSS, is a particularly important topic for investigation using independent samples of LRGs. Sawangwit et al. (2010) also detected the ISW effect in three magnitude-limited galaxy samples ($18 < r < 19$, $19 < r < 20$, and $20 < r < 21$), peaking in redshift at $z \approx 0.20$, 0.27, and 0.36, providing some confirmation of the ISW measurements in the two lower redshift LRG samples but not in the third, highest redshift, sample.

In this work, we measure the ISW signal in the cross-correlation of similar samples of galaxies to those of Sawangwit et al. (2010) but now selected from the VST ATLAS Survey (Shanks et al. 2015), with the *Planck* CMB temperature map (Planck Collaboration IX 2016a). The VST ATLAS survey has the advantage of covering large areas ($\sim$4070 deg^2) of the previously unexplored Southern sky, making it an ideal data set for improving ISW constraints. This is because most of the available area in the North has already been covered by SDSS and, since the ISW signal weakens beyond $z \approx 1$, there is limited option to increase the signal at larger distances. Indeed, with these Southern VST ATLAS data we may be approaching the upper limit to the significance of ISW detection due to cosmic variance in our limited 'local' volume (see Francis & Peacock 2010).

VST ATLAS is thus located wholly in the Southern hemisphere and is split into two areas by the Galactic plane. In the Northern Galactic Cap (NGC), the survey covers an area of $\sim 1450\,\mathrm{deg}^2$, while the Southern Galactic Cap (SGC) covers an area of $\sim 2620\,\mathrm{deg}^2$. In these regions, the survey provides imaging data in *ugriz* bands to similar depths as SDSS in the North, but with superior seeing. We shall use these data to select three LRG samples and three magnitude limited samples, closely analogous to those created by Sawangwit et al. (2010) using SDSS.

In order to test our LRG selections, we shall first compare the angular autocorrelation functions of our VST ATLAS LRG samples to those of Sawangwit et al. (2011). After cross-checking our photometric selections, we shall perform the ISW measurements and combine our results with those of Sawangwit et al. (2010), to obtain better constraints on the ISW effect at each redshift. As a further verification of the SDSS ISW measurements at $\bar{z} = 0.35$, $\bar{z} = 0.55$, and $\bar{z} = 0.68$ we repeat the measurements using the LOWZ and CMASS LRG samples from Data Release 12 (DR12; Alam et al. 2015) of the SDSS BOSS survey and the eBOSS DR14 LRG sample (Prakash et al. 2016), respectively. Unlike photometrically selected samples, these spectroscopically confirmed samples do not suffer from contamination due to stars, or from galaxies outside the redshift range, making them ideal data sets for further testing the SDSS photometric ISW measurements, in particular. We note, however, that while spectroscopic samples are not affected by stellar contamination or systematics related to photometric redshifts, they are not immune to targeting systematics that could introduce artificial correlations between the inferred density field and factors including stellar density, fibre collisions, and observing conditions. In this work, when using spectroscopic samples, we account for these potential systematics by applying the BOSS/eBOSS weights (where available), as described in Section 3.2.

To test the robustness of our ISW detections, we perform rotation tests similar to those previously implemented by Sawangwit et al. (2010) and Giannantonio et al. (2012), where the ISW cross-correlation measurement is performed on incremental rotations of the LRG overdensity maps with respect to the CMB map to test for systematics. In their analysis, Sawangwit et al. (2010) found that in approximately one to two out of eight cases, the rotated maps produce a more significant ISW detection than the unrotated map. Using a similar approach, Giannantonio et al. (2012) claimed that the results of their rotation tests were consistent with the statistical variance of their associated data sets. Here, we shall apply the rotation test to the ISW measurements obtained from the BOSS LOWZ and CMASS spectroscopic LRG samples, to check their robustness and compare our findings with those of Giannantonio et al. (2012).

Hence, our aims are first to use ATLAS to test the reproducibility of the ISW measurements in the three LRG and the three magnitude-limited galaxy samples as selected by Sawangwit et al. (2010) in SDSS. Of particular interest, is whether the VST ATLAS data independently reproduce the null detection of the ISW effect in the highest redshift LRG sample at $\bar{z} = 0.68$. Our second aim is to check the robustness of the previous SDSS LRG results using new spectroscopically confirmed SDSS LRG samples, particularly in the two lower redshift ranges. The final aim is to apply the rotation test to the BOSS LRG samples to assess the robustness of such ISW measurements.

The layout of this paper is as follows: we present a description of the selected data sets in Section 2, followed by an outline of all relevant methodology in Section 3. We present the results of our analysis and a discussion of our findings in Section 4 and conclude this work in Section 5.

Throughout this work all magnitudes are given in the AB system, and for consistency, we assume the fiducial ΛCDM cosmology adopted by Sawangwit et al. (2010) with $\Omega_\Lambda = 0.7$, $\Omega_\mathrm{m} = 0.3$, $f_\mathrm{baryon} = 0.167$, $\sigma_8 = 0.8$, and $h = 0.7$.

2 DATA SETS

2.1 *Planck* 2016 CMB temperature map

In our ISW analysis, we use the full *Planck* 2016 COMMANDER CMB temperature map (described in Planck Collaboration IX 2016a), downgraded to a HEALPIX[1] (Górski et al. 2005) resolution of $N_\mathrm{side} = 512$ (FWHM = 20 arcmin). This is consistent with the HEALPIX

[1] http://healpix.sourceforge.net

Downloaded from https://academic.oup.com/mnras/article-abstract/493/4/4830/5766327 by University of Durham user on 20 March 2020

resolution used in the analysis of Sawangwit et al. (2010). We apply the associated COMMANDER 'confidence' mask to remove sections of the sky where the temperature and polarization CMB solution cannot be trusted. The masked *Planck* CMB maps corresponding to coverage area of VST ATLAS Northern and Southern Galactic Caps are shown in Fig. 5. In this Figure, we also show the overdensity maps for our $\bar{z} = 0.68$ LRG and $20 < r < 21$ magnitude-limited galaxy sample, as described in Sections 2.2.3 and 2.2.4, respectively. Here, we show the overdensity maps of our faintest and highest redshift samples, as they are the most challenging to obtain due to their susceptibility to residual stellar contamination and artificial inhomogeneities caused by factors such as varying observing conditions.

2.2 VST ATLAS luminous red galaxies

The VST ATLAS catalogues are available from the Cambridge Astronomy Survey Unit (CASU)[2] and include $\sim 5\sigma$ detections with Kron, Petrosian, fixed aperture fluxes, and morphological classification for objects in each band as well as various other parameters.[3] Details of the VST ATLAS calibration can be found in Shanks et al. (2015) and improved global photometric calibration based on the *Gaia* survey (Gaia Collaboration 2018) is provided with the fourth Data release (DR4) of the survey.[4]

Unlike SDSS, model magnitudes are not currently available for the VST ATLAS survey and we utilize aperture magnitudes in defining our LRG photometric selections. We denote aperture magnitudes corresponding to the ATLAS Aperture flux 3 and Aperture flux 5 using subscripts 'A3' and 'A5'. These apertures have radii of 1 and 2 arcsec, respectively, and we apply their associated aperture corrections labelled as APCOR in the CASU catalogue (see footnote 3). For *g*, *r*, *i*, and *z* bands, the mean values of APCOR3 are 0.45, 0.42, 0.35, and 0.38 mag, while mean values of APCOR5 are 0.12, 0.12, 0.11, and 0.12 mag. Although these aperture corrections are derived for stars, they also provide a first-order seeing correction for faint galaxies, and overall, we find that aperture magnitudes appear to give the most consistent galaxy colours compared to SDSS model magnitudes. Where Kron magnitudes are used, we correct these to total magnitude for galaxies, based on the offset between the ATLAS Kron and SDSS model magnitudes, adding corrections of -0.28 and -0.35 mag to ATLAS $r_{\rm Kron}$ and $i_{\rm Kron}$, respectively. We correct all magnitudes for Galactic dust extinction $A_x = C_x E(B-V)$, with x representing a filter (*griz*), taking the SDSS C_x values presented in Schneider et al. (2007) (3.793, 2.751, 2.086, and 1.479 for *griz*, respectively) and using the *Planck* $E(B-V)$ map (Planck Collaboration XI 2014).

Following the photometric selection criteria of Sawangwit et al. (2010), which was used to extract LRGs from the SDSS Data Release 5 (DR5; Adelman-McCarthy et al. 2007) data, we use the VST ATLAS survey to define three LRG samples at low ($\bar{z} = 0.35$), intermediate ($\bar{z} = 0.55$), and high ($\bar{z} = 0.68$) redshifts. Sawangwit et al. (2010) in turn adopted their selection criteria based on those of the SDSS LRG (Eisenstein et al. 2001), 2DF-SDSS LRG and QSO (2SLAQ; Cannon et al. 2006), and Anglo-Australian Telescope (AAT)-AAOmega (Ross et al. 2008) spectroscopic redshift surveys, corresponding to the low-, intermediate-, and high-redshift LRG samples, respectively. In Appendix A, we compare the ATLAS and SDSS $g-r$, $r-i$, and $i-z$ colours, finding a reasonably tight scatter with no major systematic offsets in all cases. This enables us to adopt the above mentioned SDSS-based photometric selection criteria in defining our redshift limited ATLAS LRG samples. Furthermore, we remove objects located close to bright stars by matching to the Tycho-2 bright star catalogue (Høg et al. 2000). This is done to mask the haloes formed in these regions due to reflections from bright stars which could be misclassified as galaxies, when source extraction is performed on the images. Based on visual inspection of these haloes, we systematically mask circular regions around the stars with radii depending on the stars' V_T magnitudes: $V_T \leq 8$: 340 arcsec; $8 < V_T \leq 9$: 80 arcsec; $9 < V_T \leq 10$: 45 arcsec; $10 < V_T \leq 11$: 30 arcsec; $V_T > 11$: 20 arcsec.

As observations for the VST ATLAS survey are taken in one band at a time and the telescope has a 1 deg^2 field of view (henceforth referred to as a 'tile'), it is possible that different bands are observed on separate nights with varying atmospheric conditions. Although ATLAS has a relatively tight seeing distribution, in a small number of cases, variations in seeing could result in fewer objects being detected in one band (especially at fainter magnitudes). This is because unlike SDSS, forced photometry is currently unavailable for the VST ATLAS catalogue and in this work we only have access to colours for objects with $>5\sigma$ detection in each band. Consequently, when the selection is applied, regions of the sky covered by these tiles will appear underdense. Conversely, a few tiles could have a much higher than average number density due to residual stellar contamination (particularly in the NGC where the edge of the survey approaches the Galactic plane).

In order to reduce the impact of these factors on our clustering measurements, we impose a lower and an upper limit on the number of objects per tile, which masks any significantly underdense and overdense tiles. This ensures the LRG samples used in our cross-correlation analysis do not contain artificial inhomogeneities due to photometric artefacts or residual stellar contamination. We select these lower and upper limits based on comparing the autocorrelation function of the LRG samples to the measurements of Sawangwit et al. (2011), thus ensuring that such artefacts and contaminations do not impact our ability to recover the true clustering of the LRGs.

2.2.1 $\bar{z} = 0.35$ *low-redshift LRG sample*

Objects in our low-redshift LRG sample are selected based on satisfying the following conditions:

$$17.5 < r_{\rm Kron} < 19.2, \tag{1}$$

$$r_{\rm Kron} < 13.1 + c_{\parallel}/0.3, \tag{2}$$

$$c_{\perp} < 0.2, \tag{3}$$

corresponding to 'Cut I' of Eisenstein et al. (2001), or 'Cut II' of the same study as defined by

$$17.5 < r_{\rm Kron} < 19.5, \tag{4}$$

$$c_{\perp} > 0.45 - (g_{\rm A5} - r_{\rm A5})/6, \tag{5}$$

$$g_{\rm A5} - r_{\rm A5} > 1.3 + 0.25(r_{\rm A5} - i_{\rm A5}). \tag{6}$$

The colour variables $c_{\shortparallel}$ are and $c_{\perp}$ are given by

$$c_{\parallel} = 0.7(g_{\rm A5} - r_{\rm A5}) + 1.2(r_{\rm A5} - i_{\rm A5} - 0.18), \tag{7}$$

[2] http://casu.ast.cam.ac.uk/

[3] http://casu.ast.cam.ac.uk/surveys-projects/vst/technical/catalogue-generation

[4] https://www.eso.org/sci/publications/announcements/sciann17211.html

Downloaded from https://academic.oup.com/mnras/article-abstract/493/4/4830/5766327 by University of Durham user on 20 March 2020

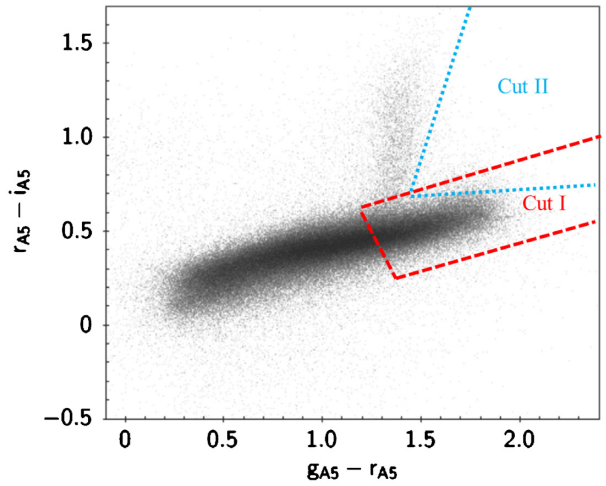

Figure 1. Our $\bar{z} = 0.35$ LRG photometric selection, based on 'Cut I' and 'Cut II' of Eisenstein et al. (2001), used in photometric selection of SDSS LRGs. Here, as in subsequent plots, the colour gradient illustrates the density of the points, with darker shades representing a higher number of data points occupying a region of the colour space. The objects shown in this plot are classified as galaxies based on their VST ATLAS *r*-band morphological classification and lie within a magnitude limit of $17.5 < r_{\rm Kron} < 19.5$.

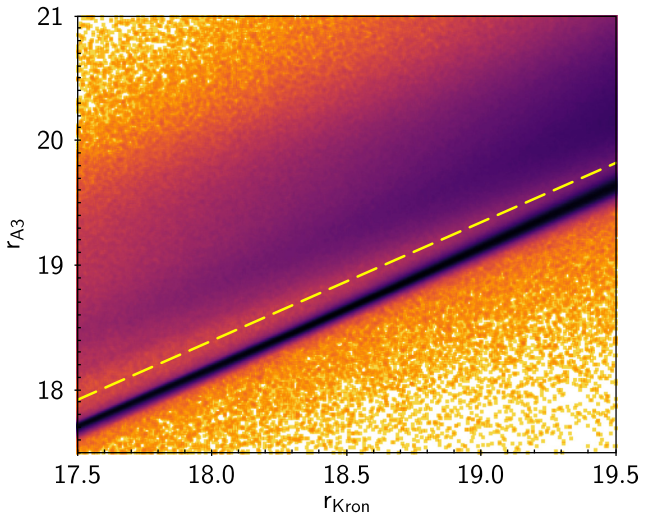

Figure 2. Further removal of residual stellar contamination from our $\bar{z} = 0.35$ LRG sample. The dashed line is described by equation 9, separating the stars (below the line) from galaxies (above the line).

$$c_{\perp} = (r_{\rm A5} - i_{\rm A5}) - (g_{\rm A5} - r_{\rm A5})/4.0 - 0.18. \quad (8)$$

We note that our use of SDSS cuts in our LRG sample selection is justified given the similarity between ATLAS and SDSS bands (see Fig. A1 for comparison of ATLAS and SDSS colours). Fig. 1 shows the cuts used to selected our $\bar{z} = 0.35$ LRG sample in the $r - i$ versus $g - r$ colour space.

To restrict our sample to galaxies, we require the CASU *r*-band morphological classification `Classification_r` = 1, remove noisy regions (due to remaining ghost reflections from bright stars or large galaxies) by requiring `sky_rms_r` < 0.2. We further remove residual stellar contamination via visual inspection of the $r_{\rm A3}$ versus $r_{\rm kron}$ diagram (see Fig. 2) by requiring

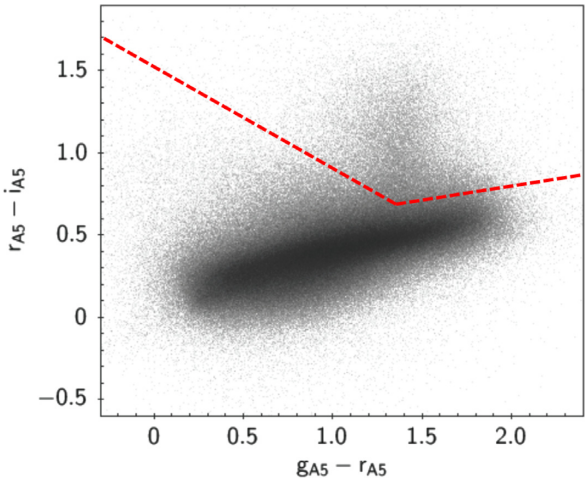

Figure 3. Our $\bar{z} = 0.55$ LRG photometric selection, following the colour cuts of Cannon et al. (2006) used in the selection of the 2SLAQ LRG sample. The objects shown here are classified as galaxies based on their VST ATLAS *i*-band morphological classification and lie within a magnitude limit of $17.5 < i_{\rm Kron} < 19.8$.

$$r_{\rm A3} > 0.909 r_{\rm kron} + 2. \quad (9)$$

In the case of our low-redshift sample, we mask tiles with fewer than 5 deg^{-2} and more than 100 deg^{-2} LRGs. This results in the removal of 10 tiles in the NGC and 8 in the SGC, leaving 31 531 ($\sim$22 deg^{-2}) and 63 245 ($\sim$24 deg^{-2}) LRGs in the NGC and SGC, respectively.

2.2.2 $\bar{z} = 0.55$ *intermediate-redshift LRG sample*

We select our intermediate-redshift LRG sample based on the following criteria that is an adaption of the photometric cuts of Cannon et al. (2006) used in the selection of the 2SLAQ LRG sample (see Fig. 3):

$$17.5 \leq i_{\rm Kron} < 19.8, \quad (10)$$

$$c_{\parallel} \geq 1.6, \quad (11)$$

$$d_{\perp} > 0.55, \quad (12)$$

$$0.5 \leq (g_{\rm A5} - r_{\rm A5}) \leq 3.0, \quad (13)$$

$$(r_{\rm A5} - i_{\rm A5}) < 2, \quad (14)$$

where $c_{\shortparallel}$ is defined in equation (7) and $d_{\perp}$ is given by

$$d_{\perp} = (r_{\rm A5} - i_{\rm A5}) - (g_{\rm A5} - r_{\rm A5})/8. \quad (15)$$

We restrict our selection to galaxies using the CASU *i*-band morphological classification (`Classification_i` = 1), limit `sky_rms_i`<0.2, and remove residual stellar contamination by imposing

$$i_{\rm A3} > 0.8 i_{\rm kron} + 4.4, \quad (16)$$

in the NGC for $i_{\rm kron} < 19.6$ and in the SGC for $i_{\rm kron} < 19.1$, while imposing

$$i_{\rm A3} > 1.3 i_{\rm kron} - 4.95 \quad (17)$$

for the NGC in the range $i_{\rm kron} > 19.6$ and

$$i_{\rm A3} > 1.8 i_{\rm kron} - 14.7 \quad (18)$$

Downloaded from https://academic.oup.com/mnras/article-abstract/493/4/4830/5766327 by University of Durham user on 20 March 2020

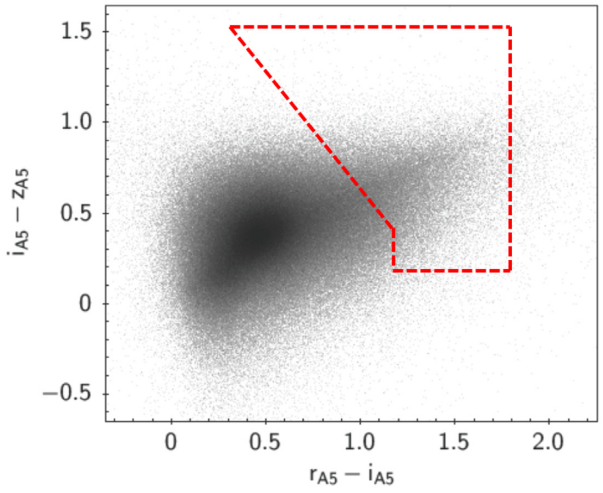

Figure 4. Our $\bar{z} = 0.68$ LRG photometric selection, following the colour cuts of Ross et al. (2008) used in the selection of the AAOmega LRG sample. The objects shown here are classified as galaxies based on their VST ATLAS *i*-band morphological classification and lie within a magnitude limit of $19.8 < i_{\rm Kron} < 20.5$.

for the SGC in the range $i_{\rm kron} > 19.1$. Here, we require different slopes for removing residual stars in the NGC compared to the SGC, as the edge of the survey lies closer to the Galactic plane in the NGC resulting in an increase in the level of contamination from residual stars.

We mask tiles with fewer than 10 and more than 130 LRGs in the NGC and those with fewer than 10 and more than 150 LRGs in the SGC. This results in the removal of 21 tiles in the NGC and 8 tiles in the SGC, leaving 78 102 ($\sim$55 deg^{-2}) and 172 744 ($\sim$66 deg^{-2}) LRGs in the NGC and SGC, respectively.

2.2.3 $\bar{z} = 0.68$ *high-redshift LRG sample*

The high-redshift LRG sample is selected based on the following criteria (see Fig. 4):

$$19.8 < i_{\rm Kron} < 20.5, \tag{19}$$

$$e_{\parallel} \geq 1.95, \tag{20}$$

$$0.5 \leq (r_{\rm A5} - i_{\rm A5}) \leq 1.8, \tag{21}$$

$$0.6 \leq (i_{\rm A5} - z_{\rm A5}) \leq 1.5, \tag{22}$$

or

$$0.2 \leq (i_{\rm A5} - z_{\rm A5}) \leq 0.6, \tag{23}$$

$$x \leq (r_{\rm A5} - i_{\rm A5}) \leq 1.8, \tag{24}$$

with x being the smaller of $e_{\parallel} = (i_{\rm A5} - z_{\rm A5}) + (9/7)(r_{\rm A5} - i_{\rm A5})$ or 1.2 at a given $(i_{\rm A5} - z_{\rm A5})$. The sample is restricted to galaxies using the CASU *i*-band morphological classification (`Classification_i` = 1) and stellar contamination is removed by imposing

$$i_{\rm A3} > 1.2 i_{\rm kron} - 3.45, \tag{25}$$

in the NGC for $i_{\rm kron} < 20.02$, otherwise

$$i_{\rm A3} > 1.4 i_{\rm kron} - 7.42. \tag{26}$$

In the SGC, the imposed cuts are

$$i_{\rm A3} > 1.2 i_{\rm kron} - 3.55, \tag{27}$$

for $i_{\rm kron} < 20.23$, otherwise

$$i_{\rm A3} > 1.4 i_{\rm kron} - 7.55. \tag{28}$$

For this sample, we mask tiles with fewer than 10 and more than 90 LRGs in both NGC and SGC. This excludes 101 tiles in the NGC and 192 in the SGC, leaving 62 379 ($\sim$46 deg^{-2}) and 138 977 ($\sim$57 deg^{-2}) LRGs in the NGC and SGC, respectively.

2.2.4 *Magnitude-limited galaxy samples*

To select our three magnitude-limited galaxy samples, we require objects to be classified as galaxies using the CASU *r*-band morphological classification (`Classification_r` = 1). We then simply select objects satisfying $18 < r_{\rm kron} < 19$, $19 < r_{\rm kron} < 20$, and $19 < r_{\rm kron} < 20$. In all cases, we apply the additional cut of $r_{\rm A5} > 0.94 r_{\rm kron} + 1.08$ to remove any residual stellar contamination from our samples. For the $18 < r_{\rm kron} < 19$ sample this results in 507 813 ($\sim$350 deg^{-2}) and 839 208 ($\sim$320 deg^{-2}) galaxies in the NGC and SGC, respectively, with the $19 < r_{\rm kron} < 20$ sample containing 1567 450 ($\sim$1100 deg^{-2}) galaxies in the NGC and 2589 744 ($\sim$1000 deg^{-2}) galaxies in the SGC. For the $19 < r_{\rm kron} < 20$ sample, we find 6072 488 ($\sim$2314 deg^{-2}) and 3522 801 ($\sim$2426 deg^{-2}) galaxies in the NGC and SGC. The mean redshift of our 18–19, 19–20, and 20–21 magnitude limited samples are $\bar{z} \approx 0.20 \pm 0.09$, 0.27 ± 0.13, and 0.36 ± 0.16, respectively.

2.3 BOSS DR12 LOWZ, CMASS and eBOSS DR14 LRG samples

The LOWZ samples covers an area of $\sim$8337 deg^2 with a number density of $\sim$38 deg^{-2}. As $z \lesssim 0.4$ LRGs were targeted in the LOWZ sample, we remove the lower redshift objects by imposing a redshift cut of $z > 0.23$, thus achieving a subset of the LOWZ sample with a mean redshift of $\bar{z} = 0.35$. The CMASS sample covers an area of $\sim$9376 deg^2 with a number density of $\sim$91 deg^{-2} and an effective redshift of $z \approx 0.57$. A full description of the target selection criteria for these samples is provided by Reid et al. (2016).

The eBOSS LRG target selection is fully described in Prakash et al. (2016), with the sample used here containing $\sim$141 000 LRGs, covering an area of $\sim$1670 deg^2, resulting in an LRG number density of $\sim$84 deg^{-2} with a median redshift of $z \approx 0.7$. A summary of the above information for our BOSS and eBOSS LRG samples is provided in Table 1.

3 METHODOLOGY

3.1 Measuring LRG angular autocorrelation function

We measure the angular correlation function $\omega(\theta)$ of our LRG samples using the Landy–Szalay estimator (Landy & Szalay 1993)

$$\omega(\theta) = 1 + \left(\frac{N_{\rm r}}{N_{\rm d}}\right)^2 \frac{DD(\theta)}{RR(\theta)} - 2\left(\frac{N_{\rm r}}{N_{\rm d}}\right) \frac{DR(\theta)}{RR(\theta)}, \tag{29}$$

where $DD(\theta)$, $DR(\theta)$, and $RR(\theta)$ are data–data, data–random, and random–random pair counts at an angular separation of θ. We perform this calculation using the CUTE[5] algorithm (Alonso 2012).

[5] https://github.com/damonge/CUTE

Downloaded from https://academic.oup.com/mnras/article-abstract/493/4/4830/5766327 by University of Durham user on 20 March 2020

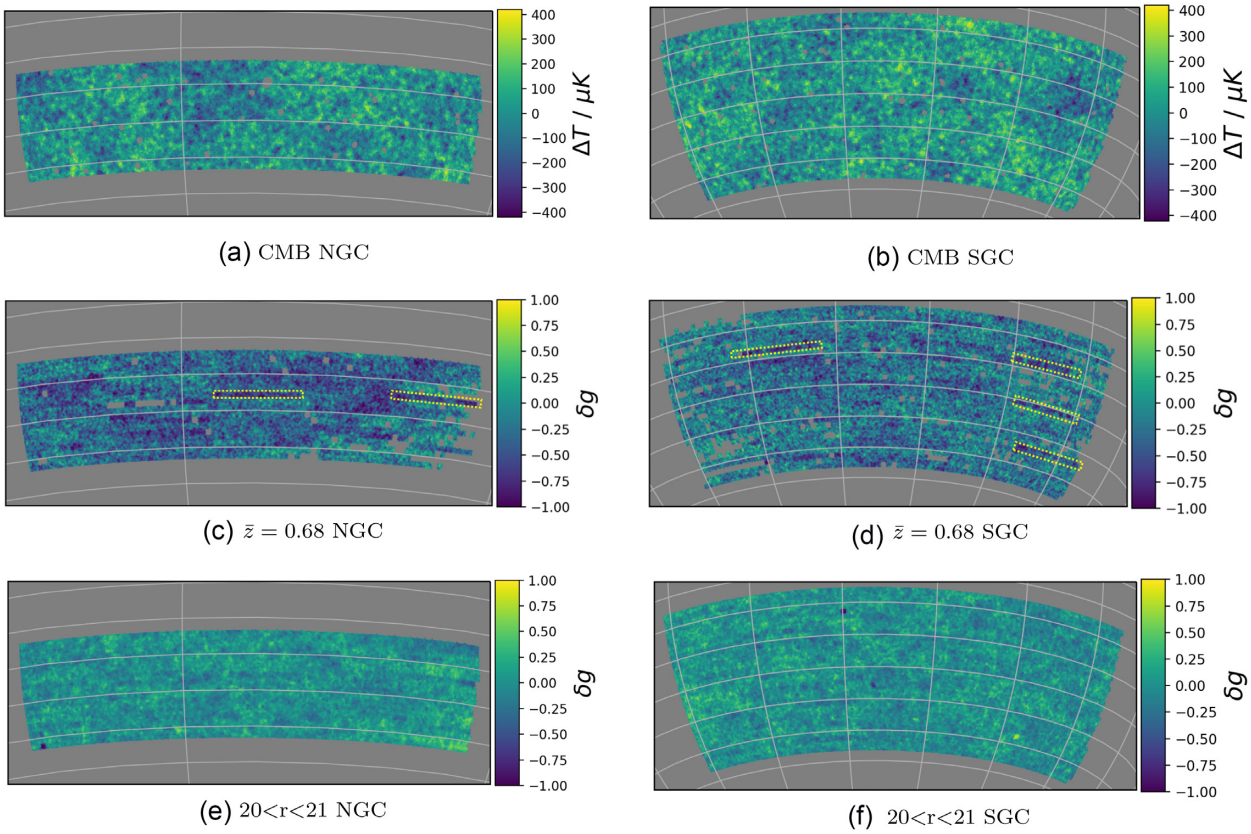

Figure 5. The *Planck* CMB temperature anisotropy map covering the NGC (a) and SGC (b) of the VST ATLAS survey (described in Section 2.1). (c and d) The VST ATLAS $\bar{z} = 0.68$ LRG overdensity maps. Although we have included a number of underdense concatenations in the final sample (marked by dotted boxes), our tests show that our auto- and cross-correlation measurements are insensitive to masking these. (e and f) The VST ATLAS galaxy overdensity maps for our $20 < r < 21$ magnitude limited sample (described in Section 2.2.4).

Table 1. Details of the VST ATLAS, BOSS LOWZ and CMASS, and eBOSS LRG samples used in our cross-correlation analyses. For comparison, we have included the same information for the SDSS LRG samples used in the analysis of Sawangwit et al. (2010).

Sample ($\bar{z}$)	Number of LRGs	Masked area (deg^2)	Sky density (deg^{-2})	Magnitude (AB)
ATLAS (0.35)	94 776	≈4060	≈23	$17.5 < r < 19.5$
ATLAS (0.55)	250 846	≈4050	≈62	$17.5 < i < 19.8$
ATLAS (0.68)	201 356	≈3800	≈53	$19.8 < i < 20.5$
SDSS (0.35)	106 699	≈8210	≈13	$17.5 < r < 19.5$
SDSS (0.55)	655 775	≈7715	≈85	$17.5 < i < 19.8$
SDSS (0.68)	800 346	≈7622	≈105	$19.8 < i < 20.5$
LOWZ (0.32)	313 446	≈8337	≈38	$16.0 < r < 19.6$
CMASS (0.57)	849 637	≈9376	≈91	$17.5 < i < 19.9$
eBOSS (0.70)	141 000	≈1670	≈84	$19.9 < i < 21.8^a$

[a]Other magnitude limits used in the selection of the eBOSS sample can be found in Prakash et al. (2016).

The correlation function is calculated up to $\theta = 100$ arcmin (using 19 logarithmically spaced bins), to match the range covered by Sawangwit et al. (2011) and allow for the comparison of the two results. For each sample, we generate random catalogues with 20× the mean number density of LRGs in the NGC and SGC and apply the same masks as applied to the data.

In order to obtain an estimate of the errors on the correlation functions, we divide each sample into $N_s = 6$ non-overlapping subsamples (with 2 in the NGC and 4 in the SGC), each ∼668 deg^2 in area. The mean number of LRGs in each subsample are ∼15 800, ∼41 800, and ∼33 600 for our $\bar{z} = 0.35, 0.55$, and 0.68 samples, respectively. We then calculate the mean of these measurements, $\bar{\omega}(\theta)$, for each sample and simply take the standard error on the mean $\sigma_{\bar{\omega}(\theta)}$, as the uncertainty on the correlation function

$$\sigma_{\bar{\omega}(\theta)} = \frac{\sigma_{N_s-1}}{\sqrt{N_s}} = \sqrt{\frac{\sum(\omega_i(\theta) - \bar{\omega}(\theta))^2}{N_s^2 - N_s}}. \quad (30)$$

Here, the sample standard deviation σ_{N_s-1} is normalized to $N_s - 1$ (as the mean is determined from the same data set, reducing the number of degrees of freedom by one), and $\omega_i(\theta)$ is the correlation function of the i-th subsample.

Downloaded from https://academic.oup.com/mnras/article-abstract/493/4/4830/5766327 by University of Durham user on 20 March 2020

3.2 Measuring LRG–CMB cross-correlation

We adopt a similar approach to Sawangwit et al. (2010) in calculating the LRG–CMB cross-correlation, a summary of which is presented here. In this work, we use the NPT (*N*-point spatial statistic; Gray et al. 2004) code to perform the cross-correlation analysis. First HEALPIX (Górski et al. 2005) is used to create LRG distribution maps by dividing our LRG samples into spherical pixels of equal area, matching the resolution of our *Planck* CMB temperature map ($N_{\rm side} = 512$; FWHM = 20 arcmin). We combine our LRG mask with the *Planck* CMB temperature mask and apply it to both the LRG distribution and CMB temperature maps.

The LRG distribution map is then used to calculate the LRG number overdensity, $\delta_{\rm L}(\hat{n})$, per pixel

$$\delta_{\rm L}(\hat{n}) = \frac{n_{\rm L}(\hat{n}) - \bar{n}_{\rm L}}{\bar{n}_{\rm L}}, \tag{31}$$

where $n_{\rm L}$ is the number of LRGs in a given pixel and $\bar{n}_{\rm L}$ is the mean number of LRGs for the sample being studied.

In the case of CMASS and eBOSS spectroscopic samples, we include the associated weights when calculating the LRG overdensity

$$\delta_{\rm L}(\hat{n}) = \frac{n_{\rm L}(\hat{n}) - w_{\rm tot} \times \bar{n}_{\rm L}}{w_{\rm tot} \times \bar{n}_{\rm L}}, \tag{32}$$

where $w_{\rm tot} = w_{\rm systot} \times (w_{\rm cp} + w_{\rm noz} - 1)$. Here, $w_{\rm systot} = w_{\rm see} \times w_{\rm star}$ is the angular systematic weight, introduced to account for non-cosmological fluctuations in target density with stellar density and seeing, $w_{\rm cp}$ accounts for fibre collisions and $w_{\rm noz}$ corrects for redshift failures by up-weighting the nearest neighbour. A more detailed description of these weights is presented by Ross et al. (2012). We do not include any weights when measuring the ISW amplitude using the LOWZ sample, as systematic weights were not supplied with the DR12 LOWZ catalogue. As inclusion of weights does not appear to have a significant impact on our CMASS and eBOSS ISW measurements, however, the impact of weights on our LOWZ ISW measurement is also likely to be small.

We then calculate the LRG–CMB two-point angular cross-correlation function, $\omega_{\rm LC}(\theta)$, using

$$\omega_{\rm LC}(\theta) = \frac{\sum_{ij} f_i \delta_{\rm L}(\bar{n}_i) f_j \Delta_T(\hat{n}_j)}{\sum_{ij} f_i f_j}, \tag{33}$$

with f_i representing the fraction of the i-th pixel located within the unmasked area, $\hat{n_i}.\hat{n_j} = \cos(\theta)$, and Δ_T being the *Planck* CMB temperature anisotropy after removing the monopole and dipole contribution. As we are using a high pixel resolution, however, the contribution from the factors weighting for unmasked fractions become negligible, and we simplify equation (33) to $\omega_{\rm LC}(\theta) = \langle \delta_{\rm L}(\hat{n_1}) \Delta_T(\hat{n_2}) \rangle$. Here, we measure the cross-correlation function using 14 logarithmically spaced bins covering the range of $\theta < 1400$ arcmin.

In order to account for the correlation between the bins in the correlation function and obtain an accurate estimation of the significance of the results, we have to consider the full covariance matrix C_{ij} when fitting a model to the data. Ideally, the covariance matrix is calculated based on thousands of simulated mock catalogues. However, creating such mock catalogues is a complex and computationally extensive task which lies beyond the immediate scope of this work. As a result, here we follow the technique used by Sawangwit et al. (2010) and obtain the covariance matrix using the jackknife resampling technique, dividing the masked *Planck* CMB temperature and ATLAS LRG overdensity maps into 36 fields of equal area (24 in SGC and 12 in NGC). Based on these $N_{\rm JK} = 36$ jackknife subsamples are generated, omitting one field at a time. The covariance matrix is then given by

$$C_{ij} = \frac{N_{\rm JK} - 1}{N_{\rm JK}} \sum_{n=1}^{N_{\rm JK}} [(\omega_{{\rm LC},n}(\theta_i) - \bar{\omega}_{\rm LC}(\theta_i)) \times ((\omega_{{\rm LC},n}(\theta_j) - \bar{\omega}_{\rm LC}(\theta_j))], \tag{34}$$

where $\omega_{{\rm LC},n}(\theta_i)$ is the measured cross-correlation of the n-th subsample, $\bar{\omega}_{\rm LC}(\theta_i)$ is the mean of the measurements from all subsamples and i and j denote the i-th and j-th bins. The $N_{\rm JK} - 1$ factor is required in order to account for the fact that the subsamples are not independent and the uncertainty on each angular bin of the cross-correlation function $\sigma_{\omega_{\rm LC}}(\theta)$, is given by the square root of the diagonal elements of the covariance matrix.

For each of our samples, we obtain separate measurements of $\omega_{\rm LC}(\theta)$ in the NGC and SGC which are combined by taking the weighted mean $\hat{\omega}_{\rm LC}(\theta)$, of the two measurements

$$\hat{\omega}_{\rm LC}(\theta) = \frac{\sum_m \omega_{{\rm LC},m}(\theta)/\sigma^2_{\omega_{{\rm LC},m}(\theta)}}{\sum_m 1/\sigma^2_{\omega_{{\rm LC},m}(\theta)}}, \tag{35}$$

where m denotes the measurement from NGC/SGC and the error on the weighted mean $\sigma_{\hat{\omega}_{\rm LC}(\theta)} = \sqrt{1/\sum_m 1/\sigma^2_{\omega_{{\rm LC},m}(\theta)}}$.

Given that our samples cover the same range of redshifts as those of Sawangwit et al. (2010), and we have assumed the same fiducial cosmology, in this work we do not generate independent theoretical predictions for the ISW signal. Instead, we simply compare our results with the models calculated in section 3 of Sawangwit et al. (2010) based on ΛCDM predictions.

Using the covariance matrix, we can then calculate the χ^2 parameter providing a statistical measure of the quality of the fit provided by the model to our observations. The χ^2 is given by

$$\chi^2 = [\hat{\omega}_{\rm LC,obs}(\theta) - \omega_{\rm LC,mod}(\theta)]^T C^{-1} [\hat{\omega}_{\rm LC,obs}(\theta) - \omega_{\rm LC,mod}(\theta)], \tag{36}$$

where $\hat{\omega}_{\rm LC,obs}(\theta)$ is our measured cross-correlation and $\omega_{\rm LC,\,mod}(\theta)$ is the prediction from the model.[6]

4 RESULTS AND DISCUSSION

4.1 VST ATLAS LRG angular autocorrelation function

The angular autocorrelation functions for our low-, intermediate-, and high-redshift LRG samples are presented in Fig. 6. For all three samples, we find a reasonable agreement between our results and the SDSS measurements of Sawangwit et al. (2011). In all cases, the agreement between the autocorrelation function amplitudes of the ATLAS and SDSS LRGs (and best-fitting double power-law models), is an indication of the success of our applied photometric selection criteria at extracting similar LRG samples from the VST ATLAS survey as those extracted from SDSS. Given the sensitivity of the autocorrelation function amplitude to stellar contamination, these results also show that our cuts have succeeded in efficiently reducing stellar contamination in our three LRG samples. Furthermore, even though our LRG samples have different number densities compared to those of Sawangwit et al. (2010), the agreement between the ATLAS and SDSS autocorrelation functions

[6]See Section 4.2 for a discussion of why we ultimately adopt an alternative approach to χ^2, in accessing the level of agreement between our results and the model.

Downloaded from https://academic.oup.com/mnras/article-abstract/493/4/4830/5766327 by University of Durham user on 20 March 2020

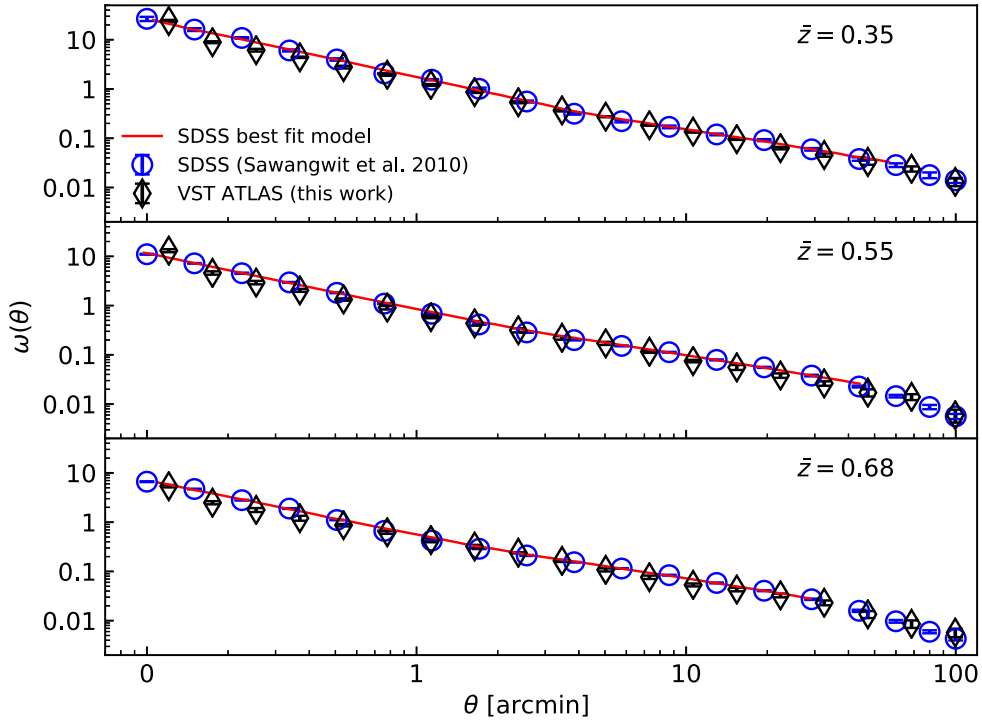

Figure 6. The VST ATLAS LRG angular autocorrelation functions, for our low-, intermediate-, and high-redshift samples (diamonds). The SDSS measurements of Sawangwit et al. (2011) (circles) and their best-fitting double power-law models (solid lines) are added for comparison. Here, the error bars are shown inside the open data points. The good agreement between the measurements from the two data sets is an indication of the success of our LRG photometric selection in limiting the samples to the correct redshift range as well as efficient removal of stellar contamination.

suggests that the LRG clustering amplitude is preserved in our samples. As a result, we do not expect our measurements of the ISW amplitude to be influenced by our different sample number densities. We believe our lower LRG densities are in part due to the slightly larger scatter in the VST ATLAS colours used in the LRG sample selections, compared to the colour scatter in SDSS. Another factor influencing our lower number density could be our additional Aperture versus Kron magnitude cuts applied to remove residual stellar contamination as described in Section 2.2.

Further tests of impact of survey systematics due to excess stellar contamination, galactic dust extinction, and variations in airmass and seeing are presented in Appendix B. Our tests indicate that these systematics do not have a significant effect on our ISW measurements.

4.2 VST ATLAS LRG–*Planck* CMB cross-correlation

Fig. 7 shows a comparison of our ISW measurements based on the cross-correlation of VST ATLAS LRGs and *Planck* CMB temperature anisotropy map, to the results of Sawangwit et al. (2010) (where the same analysis was performed using SDSS LRGs and the WMAP temperature map). We find a good agreement between the two measurements in terms of ISW amplitude at all redshifts. Our error bars are, however, larger than those of Sawangwit et al. (2010), which can be partially attributed to the $\sim 2\times$ lower sky coverage of the ATLAS survey compared to SDSS, as well as the lower number density of LRGs, at least in the case of our $\bar{z} = 0.55$ and $\bar{z} = 0.68$ samples (see Table 1).

As on large scales relevant to ISW measurements, the statistical error is limited by sample variance, one would expect the errors on our ISW measurements to scale with $\sigma_{\rm ATLAS}/\sigma_{\rm SDSS} \approx \sqrt{(A_{\rm SDSS}/A_{\rm ATLAS})}$ where A represents the area of each sample. We therefore expect the ATLAS error bars to be $\sim 1.4\times$ larger than those of SDSS. However, we find that the errors on our VST ATLAS LRG ISW measurements do not obey the above scaling with SDSS and are $\sim 1.9\times$, $\sim 2.4\times$, and $\sim 3.0\times$ larger than those from SDSS, for our $\bar{z} = 0.35$, 0.55, and 0.68 samples, respectively. Assuming the SDSS ISW errors of Sawangwit et al. (2010) are not underestimated, the reason behind the larger than expected errors on our LRG ISW measurements remains unknown.

Similarly to Sawangwit et al. (2010), when fitting our measurements to the ΛCDM model, we find the resulting χ^2 values (given by equation 36) to be unreliable. This is likely due to our use of the jackknife technique in estimating the covariance matrices (see equation 34) and the failure of this technique in accurately estimating the off-diagonal covariance matrix elements, which in turn impacts the χ^2 fitting results. As mocks are currently not available for the VST ATLAS survey (and the Bootstrap technique was also unsuccessful in improving our covariance matrix estimations), we follow the approach of Sawangwit et al. (2010) and simply assess the deviation of our measurements from the ΛCDM predictions and a null ISW amplitude, based on a single large bin covering the $12 < \theta < 120$ arcmin range.

Table 2 contains a summary of the our single bin ISW measurements, those of Sawangwit et al. (2010) and also the weighted mean of the results from the two studies (see Fig. 7b). In the case of the $\bar{z} = 0.35$ and 0.55 LRG samples, we found our detected ISW amplitude to be in agreement with the predictions of ΛCDM, supporting the late-time accelerated expansion of the Universe. As seen in Table 2, upon combining the ATLAS and SDSS measurements, at these redshifts we detect the ISW effect at 1.2σ

Downloaded from https://academic.oup.com/mnras/article-abstract/493/4/4830/5766327 by University of Durham user on 20 March 2020

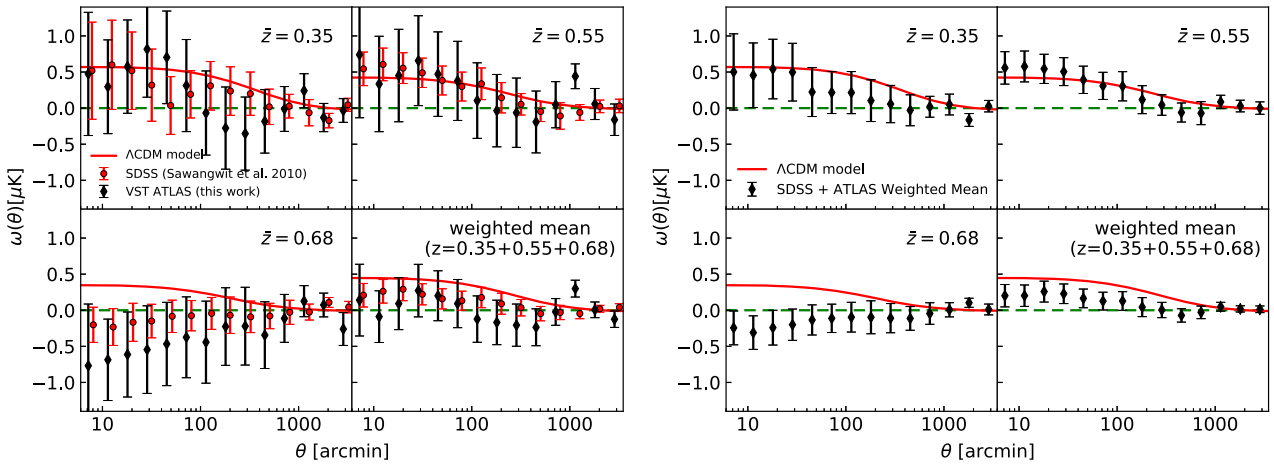

Figure 7. (a) The VST ATLAS LRG–*Planck* CMB cross-correlation signal from our low-, intermediate-, and high-redshift samples compared to SDSS LRG–WMAP CMB measurements of Sawangwit et al. (2010). The predictions of the ΛCDM model are shown by the red solid lines. (b) The weighted mean of the two measurements in (a).

Table 2. Summary of our VST ATLAS and BOSS/eBOSS LRGs–*Planck* CMB cross-correlation measurements of the ISW amplitude (based on a single bin covering the $12 < \theta < 120$ arcmin range). The SDSS LRG–WMAP CMB measurements of Sawangwit et al. (2010) and weighted mean of the results from the various data sets are also included. The final column shows the deviation of each measurement from the predictions of the ΛCDM model and a null amplitude. In all cases, we use the weighted mean to combine the results from different redshifts.

Sample	$\bar{z}$	ω(12–120 arcmin) (μK)	Deviation significance (ΛCDM, null)
VST ATLAS (This work)	0.35	0.47 ± 0.62	$(0.0\sigma, 0.8\sigma)$
	0.55	0.41 ± 0.51	$(0.1\sigma, 0.8\sigma)$
	0.68	-0.49 ± 0.59	$(1.3\sigma, 0.8\sigma)$
	$0.35 + 0.55 + 0.68$	0.11 ± 0.33	$(0.8\sigma, 0.3\sigma)$
SDSS (Sawangwit et al. 2010)	0.35	0.33 ± 0.33	$(0.5\sigma, 1.0\sigma)$
	0.55	0.44 ± 0.21	$(0.5\sigma, 2.1\sigma)$
	0.68	-0.13 ± 0.20	$(2.0\sigma, 0.6\sigma)$
	$0.35 + 0.55 + 0.68$	0.21 ± 0.14	$(1.2\sigma, 1.5\sigma)$
BOSS/eBOSS (This work)	0.35	0.32 ± 0.38	$(0.4\sigma, 0.9\sigma)$
	0.55	0.73 ± 0.38	$(1.1\sigma, 2.0\sigma)$
	0.68	0.50 ± 0.76	$(0.3\sigma, 0.7\sigma)$
	$0.35 + 0.55 + 0.68$	0.52 ± 0.25	$(0.6\sigma, 2.1\sigma)$
VST ATLAS + SDSS (Weighted mean)	0.35	0.36 ± 0.29	$(0.5\sigma, 1.2\sigma)$
	0.55	0.43 ± 0.19	$(0.5\sigma, 2.3\sigma)$
	0.68	-0.17 ± 0.19	$(2.3\sigma, 0.9\sigma)$
	$0.35 + 0.55$	0.41 ± 0.16	$(0.1\sigma, 2.6\sigma)$
	$0.35 + 0.55 + 0.68$	0.20 ± 0.12	$(1.4\sigma, 1.7\sigma)$
VST ATLAS + BOSS/eBOSS (Weighted mean)	0.35	0.36 ± 0.32	$(0.4\sigma, 1.1\sigma)$
	0.55	0.62 ± 0.31	$(0.9\sigma, 2.0\sigma)$
	0.68	-0.12 ± 0.47	$(0.8\sigma, 0.3\sigma)$
	$0.35 + 0.55$	0.49 ± 0.22	$(0.4\sigma, 2.2\sigma)$
	$0.35 + 0.55 + 0.68$	0.38 ± 0.20	$(0.1\sigma, 1.9\sigma)$

and 2.3σ (or 2.6σ combined[7] – see Fig. 8a). In the case of the $\bar{z} = 0.68$ LRG sample, however, where the ISW measurement from VST ATLAS has a similar negative amplitude to SDSS, we find a $\sim 2\sigma$ deviation from the ΛCDM prediction, when combining the results from the two studies (Fig. 8b).

[7]Based on the weighted mean of the results from the two redshifts.

In these measurements, the signal is mostly dominated by SDSS and combining the VST ATLAS and SDSS results only yields a small increase in the significance of detection (or rejection) of the ΛCDM ISW predictions, compared to the results previously obtained from SDSS alone. We note, however, that the errors in the ATLAS ISW measurements would be 50–70 per cent smaller if they had scaled correctly with sample size, which may explain the unexpectedly good agreement between SDSS and ATLAS

Downloaded from https://academic.oup.com/mnras/article-abstract/493/4/4830/5766327 by University of Durham user on 20 March 2020

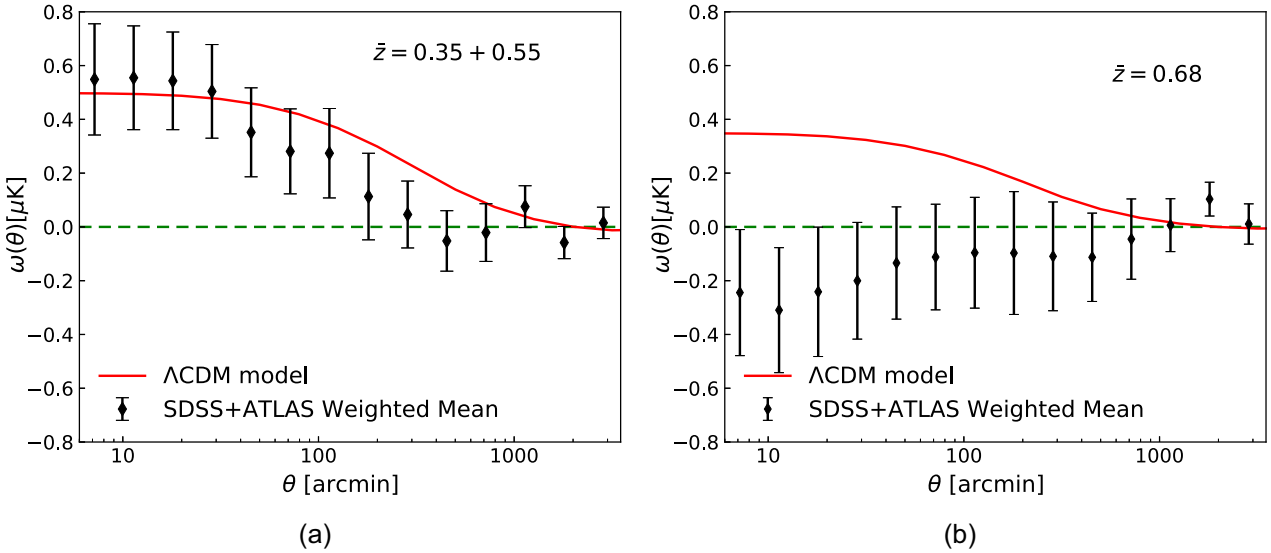

Figure 8. (a) The weighted mean of the SDSS + ATLAS ISW measurements at $\bar{z} = 0.35$ and 0.55 (i.e. the top panels of Fig. 7b). (b) The $\bar{z} = 0.68$ measurement (bottom left panel of Fig. 7b). As shown in Table 2, when combining the $\bar{z} = 0.35$ and 0.55 measurements, we detect the ISW signal at 2.6σ and we note the result is in agreement with the predictions of ΛCDM. However, at $\bar{z} = 0.68$ the ISW amplitude is close to zero and deviates from the ΛCDM predictions by 2.0σ.

results in all three redshift ranges. Overall, the results of this study offer a valuable confirmation of the measured ISW amplitudes of Sawangwit et al. (2010) based on SDSS and WMAP, using the cross-correlation of two independent data sets (VST ATLAS and *Planck*) that also cover completely separate areas of the sky.

4.3 Comparison to BOSS DR12 LOWZ, CMASS and eBOSS LRGs samples

To further verify the SDSS measurements at $\bar{z} = 0.35$, 0.55, and 0.68, we compare the results with those obtained using the LOWZ, CMASS, and eBOSS LRG redshift samples (see Section 2.3). As shown in Fig. 9(a) with the exception of the $\theta > 100$ arcmin higher BOSS ISW amplitude at $\bar{z} = 0.55$, the BOSS measurements provide a general confirmation of the SDSS results at $\bar{z} = 0.35$ and $\bar{z} = 0.55$. The $\bar{z} = 0.35$ results show particularly good agreement between the photometric and spectroscopic samples. The reason behind the higher than expected $\bar{z} = 0.55$ BOSS amplitude at large separations remains unknown. At $\bar{z} = 0.68$, the ISW amplitude is more positive in the eBOSS LRG sample than observed in SDSS or ATLAS (see Figs 9a and b). Nevertheless, the eBOSS result shows a qualitatively different form to that of the lower redshift results generally rising towards larger separations rather than falling. This behaviour is also similar to that seen in SDSS and ATLAS at the same redshift, just with a higher amplitude for eBOSS.

At $\bar{z} = 0.35$ and $\bar{z} = 0.55$, we therefore find similar results whether we combine ATLAS with SDSS photometric, or BOSS/eBOSS spectroscopic LRG samples. For example, in Table 2, at $\bar{z} = 0.35$ and 0.55, the null amplitude is rejected at 1.1σ and 2.0σ when combining the ATLAS + BOSS measurements (Fig. 9c); similar to the 1.2σ and 2.3σ ATLAS + SDSS ISW detection. When combining the measurements at $\bar{z} = 0.35$ and 0.55, the ATLAS + BOSS result rejects the null signal at 2.2σ, compared to the 2.6σ null rejection obtained from ATLAS + SDSS.

At $\bar{z} = 0.68$, however, Table 2 shows a 0.8σ deviation from ΛCDM rather than 2.3σ, when the ATLAS measurement is combined with eBOSS instead of SDSS. Similarly, the ATLAS + BOSS/eBOSS weighted mean of the results from the three redshift bins appears to be in better agreement with ΛCDM compared to ATLAS + SDSS (a 0.1σ deviation compared to 1.4σ). However, in both cases this lower rejection significance of ΛCDM is mainly due to the larger eBOSS errors, rather than any intrinsically improved agreement of the *form* of the high redshift result to the ISW model.

These larger errors on the eBOSS ISW measurements are due to its lower sky coverage than that of the equivalent SDSS LRG sample, and SDSS thus remains the $\bar{z} = 0.68$ measurement with the highest signal in this sky area. We therefore conclude that ATLAS + SDSS measurement shown in Fig. 8(b) provides the best estimate of the ISW effect using $\bar{z} = 0.68$ LRGs, in the full North + South combined sample. Similarly, in Fig. 8(a) we use the ATLAS and SDSS data to provide the best $\bar{z} = 0.35$ plus $\bar{z} = 0.55$ ISW measurement in the full North + South sample. The difference between the two appears clear, although the $\bar{z} = 0.68$ deviation significance from ΛCDM, is currently only at a moderate level of $\sim 2.3\sigma$. It is therefore important to remeasure the high-redshift ISW signal using the complete eBOSS survey, as well as future surveys such as DESI (DESI Collaboration 2016) and LSST (Ivezić et al. 2019), which will offer large, high-purity LRG samples that could assess any potential deviations from ΛCDM at a higher statistical significance.

4.4 Magnitude-limited samples

Fig. 10(a) shows a comparison of our measurements of the three *r*-band magnitude-limited samples to the SDSS measurements of Sawangwit et al. (2010). Once again a general agreement is found between the two sets of measurements. Unlike our redshift-limited LRG samples, here the number of galaxies in our three samples are in line with theoretical expectations, and we find the VST ATLAS error bars to be comparable to those of Sawangwit et al. (2010) based on SDSS, once the difference in survey areas is accounted for.

Upon combining the two sets of measurements by taking their weighted mean (see Fig. 10b), we find that on scales of 12 arcmin $< \theta <$ 120 arcmin, the null amplitude is rejected at moderate levels of

Downloaded from https://academic.oup.com/mnras/article-abstract/493/4/4830/5766327 by University of Durham user on 20 March 2020

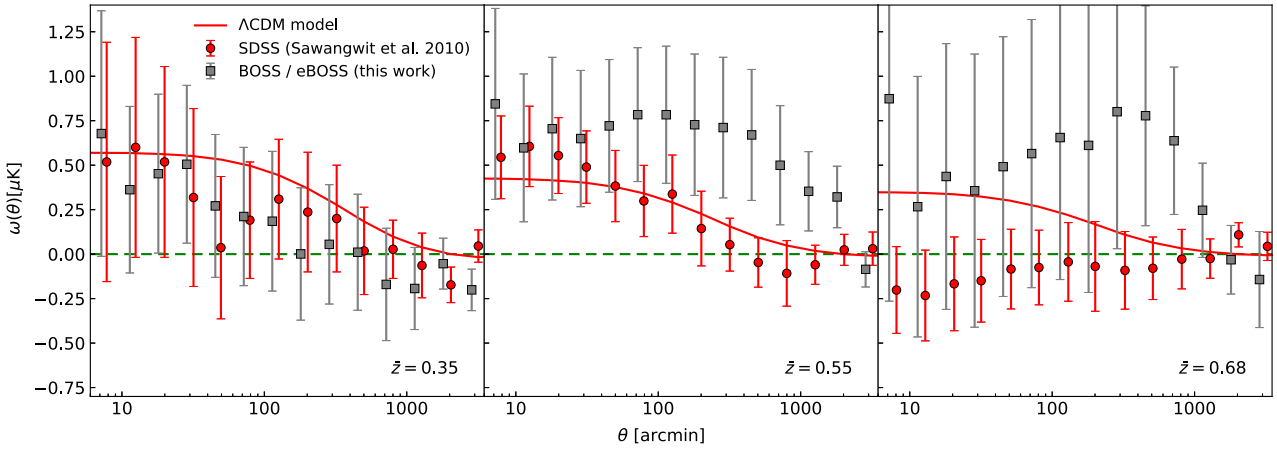

(a) SDSS versus BOSS/eBOSS.

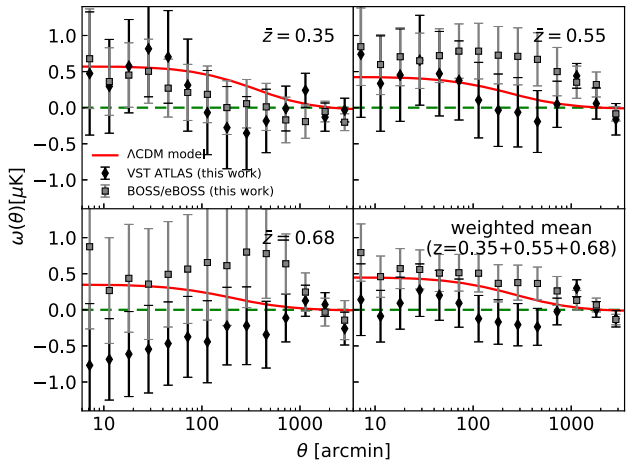

(b) VST ATLAS versus BOSS/eBOSS.

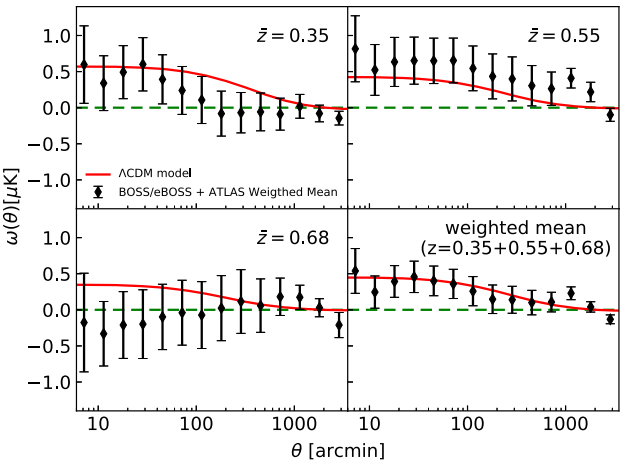

(c) VST ATLAS + BOSS/eBOSS.

Figure 9. (a) Comparison of the SDSS and BOSS/eBOSS ISW measurements. (b and c) same as (7a and b) but comparing/combining the VST ATLAS ISW measurements to those based on BOSS/eBOSS.

$\sim 1.3\sigma$, $\sim 1.9\sigma$, and $\sim 2.0\sigma$ for the $18 < r < 19$, $19 < r < 20$, and $20 < r < 21$ samples, respectively. Recalling that these samples have mean redshifts of $\bar{z} \approx 0.20 \pm 0.09$, 0.27 ± 0.13, and 0.36 ± 0.16, we note that the $\sim 2.0\sigma$ ISW detection obtained from the $20 < r < 21$ ATLAS + SDSS galaxy samples, provides a further confirmation of our 1.2σ ISW detection based on the $\bar{z} = 0.35$ ATLAS + SDSS LRG samples.

4.5 ISW rotation test

Following the approach of previous works including Sawangwit et al. (2010) and Giannantonio et al. (2012), we test for presence of systematic effects and the robustness of our measurements by rotating the LRG data with respect to the CMB map in increments of 40° about the Galactic pole (by adding 40° to the Galactic longitude). Here, we perform the rotation test on the LOWZ and CMASS samples, as they provide contamination-free samples of spectroscopically confirmed LRGs. Given the current low sky coverage and large uncertainties on the eBOSS measurement, we do not include this sample in our rotation tests.

Fig. 11(a) shows the results of our single-bin (12 arcmin $< \theta <$ 120 arcmin) rotation tests for the LOWZ and CMASS samples. Statistically, one would expect 32 and 5 per cent of the rotations to exceed the 1σ and 2σ thresholds.

In the case of the LOWZ sample, we find that 4/8 and 2/8 (50 and 25 per cent) of the rotations result in amplitudes that lie above the 1σ and 2σ thresholds, respectively. Furthermore, we find that 2/8 (25 per cent) of the rotations produce a more significant rejection of null, than the zero-rotation value.

For the CMASS sample, we find that 4/8 and 1/8 (50 and 12.5 per cent) of the points are further than 1σ and 2σ away from zero, respectively, while 1/8 (12.5 per cent) of the rotations produces a more significant null rejection than our zero-rotation result. In order to ensure the single-bin measurements in Fig. 11(a) do not appear to be artificially deviated from zero due to the presence of outliers in the full-range cross-correlation functions, in Fig. 11(b) we show the full-range cross-correlation function for the 240° rotation of the CMASS sample (which resulted in the highest deviation from zero). Here, we can see that the 240° rotation appears to have produced an ISW amplitude which is consistently high in our 12 arcmin $< \theta <$ 120 arcmin range of interest, resulting in a higher null rejection when compared to the 2σ rejection obtained from the zero-rotation CMASS result as shown in Table 2.

Downloaded from https://academic.oup.com/mnras/article-abstract/493/4/4830/5766327 by University of Durham user on 20 March 2020

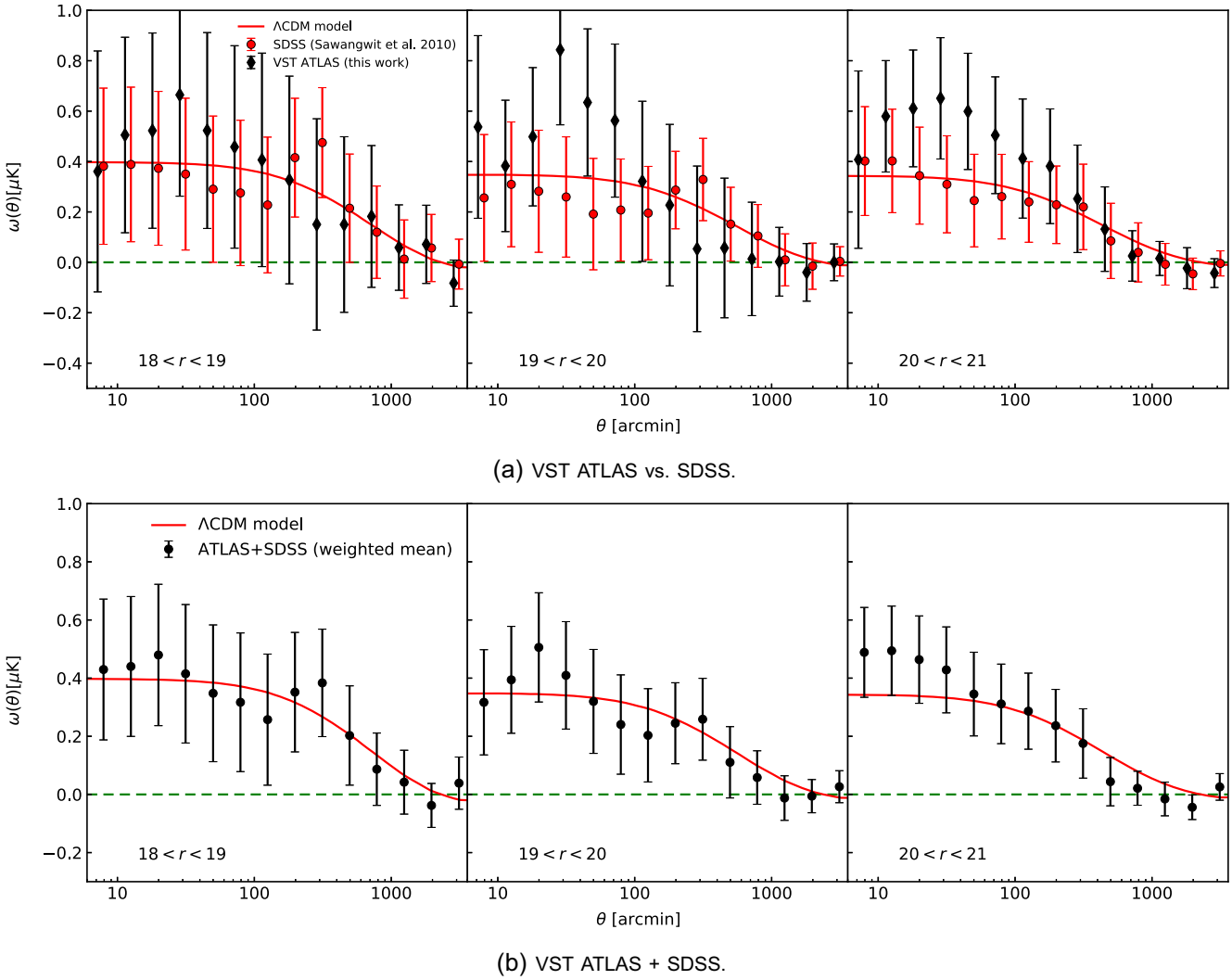

Figure 10. (a) The ISW signal from our three VST ATLAS *r*-band magnitude-limited galaxy samples (diamonds) in comparison with the SDSS results of Sawangwit et al. (2010) (circles) and ΛCDM model prediction (solid lines). (b) weighted mean of the results from the two studies. Here, the mean redshifts of the $18 < r < 19$, $19 < r < 20$, and $20 < r < 21$ samples are $\bar{z} \approx 0.20$, 0.27, and 0.36, respectively.

Here our results are in agreement with those of Sawangwit et al. (2010), who found that in one to two out of eight cases, the rotated maps produced a more significant null rejection than the zero-rotation result. However, we find our results to be in contrast to the findings of Giannantonio et al. (2012) (as shown in their table 3), where in their six studied samples only 23 and 2 per cent of their rotations exceeded the 1σ and 2σ thresholds (fully consistent with the 32 and 5 per cent statistical expectations), with none exceeding the null rejection significance of the unrotated map. Similarly, Giannantonio et al. (2012) found that across all seven samples studied by Sawangwit et al. (2010), only 39 and 11 per cent of rotations exceeded the 1σ and 2σ thresholds.

Giannantonio et al. (2012) suggest that the higher percentage of points exceeding the 1σ and 2σ thresholds, found by Sawangwit et al. (2010) could be due to their use of the jackknife method in estimating the errors, which has been shown to produce somewhat smaller errors (see Cabré et al. 2007) than those obtained from simulated mocks (as used by Giannantonio et al. 2012). This could in part also explain the higher than expected percentages found in our rotation tests. However, given that for the LOWZ and CMASS samples, 50 per cent of our rotations exceeded the 1σ threshold, 25 and 12.5 per cent exceeded the 2σ threshold, and 2/8 and 1/8 rotations produced a more significant rejection of null than the unrotated map; our findings suggest that the robustness of current ISW detections is still not completely secure even at $\bar{z} = 0.35$ and $\bar{z} = 0.55$. Consequently, as well as any remaining statistical gains, improvements in reducing systematics on ISW measurements should still be sought in future works.

5 CONCLUSIONS

We have presented our measurements of the ISW signal in the cross-correlation of the *Planck* CMB temperature map with three photometrically selected LRG samples with mean redshifts of $\bar{z} = 0.35, \bar{z} = 0.55$, and $\bar{z} = 0.68$, selected from the VST ATLAS survey. We then combine our measurements with those of Sawangwit et al. (2010), where the same analysis was performed using the WMAP CMB temperature map and LRG samples selected from SDSS.

Upon combining the measurements from ATLAS and SDSS, at $\bar{z} = 0.35$ and $\bar{z} = 0.55$, we detect the ISW signal at 1.2σ and 2.3σ, respectively (i.e. a combined detection of 2.6σ). This is in agreement with the predictions of ΛCDM supporting the late-time

Downloaded from https://academic.oup.com/mnras/article-abstract/493/4/4830/5766327 by University of Durham user on 20 March 2020

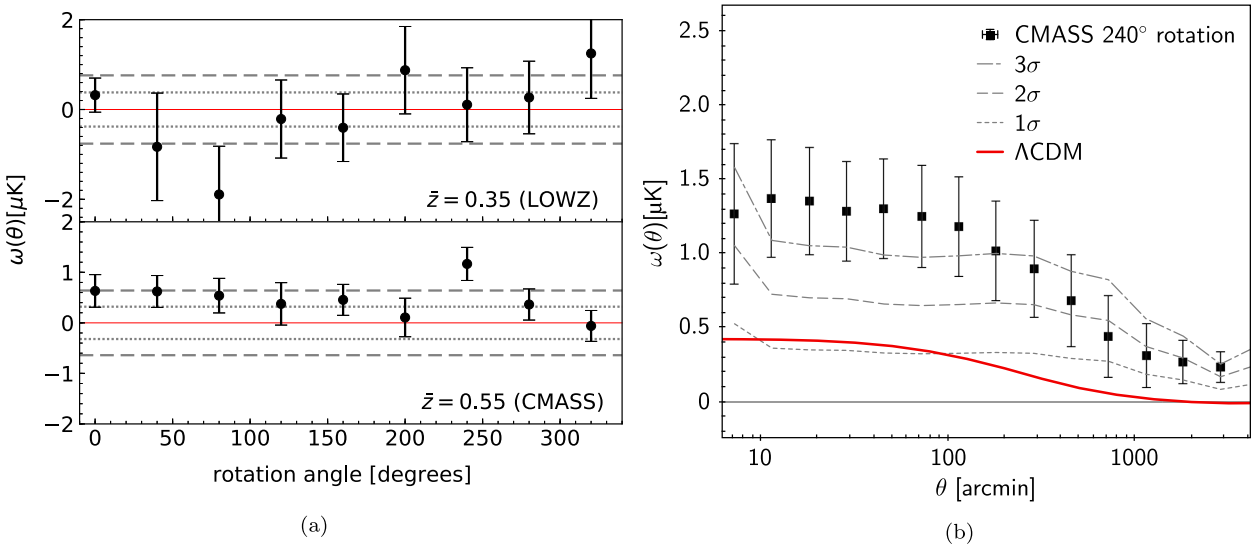

Figure 11. (a) The BOSS LOWZ and CMASS single-bin (12 arcmin $< \theta <$ 120 arcmin) ISW amplitudes as a function of rotation angles (see text for details). The 1σ and 2σ error regions around the null amplitude are shown by dotted and dashed lines. These are based on the error bars of the zero rotation data points and represent level of variance in the data. (b) The full-range 240° rotation result for the CMASS sample showing that in the in the 12 arcmin $< \theta <$ 120 arcmin range used to extract our single bin measurement, the ISW amplitude is consistently high and is not merely due to the presence of a few outliers.

accelerated expansion of the Universe. We further verify our results at these redshifts by repeating the measurements using the BOSS DR12 LOWZ and CMASS spectroscopic LRG samples. This time upon combining the ATLAS and BOSS measurements, we detect the ISW signal at 1.1σ and 2.0σ (with a combined significance of 2.2σ). Furthermore, we detect the ISW effect in three magnitude-limited galaxy samples, with mean redshifts of $\bar{z} \approx 0.20$, 0.27, and 0.36, at $\sim 1.3\sigma$, 1.9σ, and 2.0σ, respectively.

However, we do not detect the ISW signal at $\bar{z} = 0.68$ when combining the ATLAS and SDSS results. Further tests using eBOSS LRGs at this redshift remain inconclusive due to the large uncertainties, caused by the current relatively low sky coverage of the survey. If the ISW signal is shown to be inconsistent with the predictions of ΛCDM at high redshifts, it could open the door to alternative theories such as modified gravity models. It is therefore important to repeat the $z \sim 0.7$ ISW measurement upon the completion of the eBOSS survey and using data from upcoming surveys such as DESI and LSST which will provide the statistics and reduced systematics required to assess any deviations from the predictions of ΛCDM.

Finally, we test the robustness of our ISW measurements at $\bar{z} = 0.35$ and $\bar{z} = 0.55$ by rotating the LRG overdensity map with respect to the CMB temperature map in eight increments about the Galactic pole. Here, in contrast to the findings of Giannantonio et al. (2012), we find that a higher percentage of rotations result in amplitudes 1σ and 2σ away from zero than statistically expected. Furthermore, we find that in the case of LOWZ and CMASS samples 2/8 and 1/8 rotations result in more significant rejections of the null amplitude than obtained from our unrotated maps. Consequently, our results indicate that the robustness and significance of ISW detections still warrant further examination in future works. Similarly rotation tests could serve as a useful tool for determining the level of systematics in ISW measurements obtained from future surveys.

In summary, the results of this study provide a confirmation of previous ISW measurements from Sawangwit et al. (2010). However, despite the visual impressions given by the cross-correlation measurements, our detections of the ISW signal at $\bar{z} = 0.35$, $\bar{z} = 0.55$, and in three magnitude-limited samples remain at low to moderate levels of significance. However, previous works such as Francis & Peacock (2010) have demonstrated that the ISW signal could remain evasive in $\gtrsim$10 per cent of cases, even with the availability of the best possible data. None the less, given the cosmological implications of any significant deviations from the predictions of ΛCDM, repeating the ISW measurement at $z \sim 0.7$, where our results point to the possibility of such deviations, using the next generation of large sky surveys, remains a worthwhile and important endeavour.

ACKNOWLEDGEMENTS

This research made use of ASTROPY,[8] a community-developed core PYTHON package for Astronomy (Price-Whelan et al. 2018), as well as TOPCAT and STILTS[9] packages (Taylor 2005).

Funding for the Sloan Digital Sky Survey IV has been provided by the Alfred P. Sloan Foundation, the U.S. Department of Energy Office of Science, and the Participating Institutions. SDSS-IV acknowledges support and resources from the Center for High-Performance Computing at the University of Utah. The SDSS web site is www.sdss.org.

SDSS-IV is managed by the Astrophysical Research Consortium for the Participating Institutions of the SDSS Collaboration including the Brazilian Participation Group, the Carnegie Institution for Science, Carnegie Mellon University, the Chilean Participation Group, the French Participation Group, Harvard-Smithsonian Center for Astrophysics, Instituto de Astrofísica de Canarias, The Johns Hopkins University, Kavli Institute for the Physics and Mathematics of the Universe (IPMU) / University of Tokyo, the Korean Participation Group, Lawrence Berkeley National Laboratory, Leibniz Institut für Astrophysik Potsdam (AIP), Max-Planck-Institut für Astronomie (MPIA Heidelberg), Max-Planck-Institut für Astrophysik (MPA Garching), Max-Planck-Institut für

[8] http://www.astropy.org
[9] http://www.star.bris.ac.uk/mbt/topcat/sun253/index.html

Downloaded from https://academic.oup.com/mnras/article-abstract/493/4/4830/5766327 by University of Durham user on 20 March 2020

Extraterrestrische Physik (MPE), National Astronomical Observatories of China, New Mexico State University, New York University, University of Notre Dame, Observatário Nacional / MCTI, The Ohio State University, Pennsylvania State University, Shanghai Astronomical Observatory, United Kingdom Participation Group, Universidad Nacional Autónoma de México, University of Arizona, University of Colorado Boulder, University of Oxford, University of Portsmouth, University of Utah, University of Virginia, University of Washington, University of Wisconsin, Vanderbilt University, and Yale University.

RM, TS & NM acknowledge the support of the Science and Technology Facilities Council (ST/L00075X/1 and ST/L000541/1)

We would also like to thank Alina Talmantaite for her useful comments and discussion.

REFERENCES

Adelman-McCarthy J. K. et al., 2007, ApJS, 172, 634
Alam S. et al., 2015, ApJS, 219, 12
Alam S. et al., 2017, MNRAS, 470, 2617
Alonso D., 2012, preprint (arXiv:1210.1833)
Bielby R., Shanks T., Sawangwit U., Croom S. M., Ross N. P., Wake D. A., 2010, MNRAS, 403, 1261
Boughn S. P., Crittenden R. G., 2002, Phys. Rev. Lett., 88, 021302
Boughn S., Crittenden R., 2004, Nature, 427, 45
Cabré A., Gaztañaga E., Manera M., Fosalba P., Castander F., 2006, MNRAS, 372, L23
Cabré A., Fosalba P., Gaztañaga E., Manera M., 2007, MNRAS, 381, 1347
Cai Y.-C., Neyrinck M., Mao Q., Peacock J. A., Szapudi I., Berlind A. A., 2017, MNRAS, 466, 3364
Cannon R. et al., 2006, MNRAS, 372, 425
Clifton T., Ferreira P. G., Padilla A., Skordis C., 2012, Phys. Rep., 513, 1
Corasaniti P.-S., Giannantonio T., Melchiorri A., 2005, Phys. Rev. D, 71, 123521
DESI Collaboration, 2016, preprint (arXiv:1611.00036)
Dunsby P., Goheer N., Osano B., Uzan J.-P., 2010, J. Cosmol. Astropart. Phys., 6, 017
Eisenstein D. J. et al., 2001, AJ, 122, 2267
Fosalba P., Gaztañaga E., 2004, MNRAS, 350, L37
Fosalba P., Gaztañaga E., Castander F. J., 2003, ApJ, 597, L89
Francis C. L., Peacock J. A., 2010, MNRAS, 406, 2
Gaia Collaboration, 2018, A&A, 616, A1
Giannantonio T. et al., 2006, Phys. Rev. D, 74, 063520
Giannantonio T., Scranton R., Crittenden R. G., Nichol R. C., Boughn S. P., Myers A. D., Richards G. T., 2008, Phys. Rev. D, 77, 123520
Giannantonio T., Crittenden R., Nichol R., Ross A. J., 2012, MNRAS, 426, 2581
Górski K. M., Hivon E., Banday A. J., Wandelt B. D., Hansen F. K., Reinecke M., Bartelmann M., 2005, ApJ, 622, 759
Goto T., Szapudi I., Granett B. R., 2012, MNRAS, 422, L77
Granett B. R., Neyrinck M. C., Szapudi I., 2008, preprint (arXiv:0805.2974)
Granett B. R., Neyrinck M. C., Szapudi I., 2009, ApJ, 701, 414
Granett B. R., Kovács A., Hawken A. J., 2015, MNRAS, 454, 2804
Gray A. G., Moore A. W., Nichol R. C., Connolly A. J., Genovese C., Wasserman L., 2004, in Ochsenbein F., Allen M. G., Egret D., eds, ASP Conf. Ser. Vol. 314, Astronomical Data Analysis Software and Systems (ADASS) XIII. Astron. Soc. Pac., San Francisco, p. 249
Ho S., Hirata C., Padmanabhan N., Seljak U., Bahcall N., 2008, Phys. Rev. D, 78, 043519
Høg E. et al., 2000, A&A, 355, L27
Ivezić Ž. et al., 2019, ApJ, 873, 111
Kovács A., Szapudi I., Granett B. R., Frei Z., 2013, MNRAS, 431, L28
Kovács A. et al., 2017, MNRAS, 465, 4166
Landy S. D., Szalay A. S., 1993, ApJ, 412, 64
Maeder A., 2017, ApJ, 834, 194
McEwen J. D., Vielva P., Hobson M. P., Martinez-Gonzalez E., Lasenby A. N., 2006, preprint (arXiv:astro-ph/0602398)
Nadathur S., Crittenden R., 2016, ApJ, 830, L19
Nolta M. R. et al., 2004, ApJ, 608, 10
Padmanabhan N., Hirata C. M., Seljak U., Schlegel D. J., Brinkmann J., Schneider D. P., 2005, Phys. Rev. D, 72, 043525
Pápai P., Szapudi I., Granett B. R., 2011, ApJ, 732, 27
Planck Collaboration XI, 2014, A&A, 571, A11
Planck Collaboration IX, 2016a, A&A, 594, A9
Planck Collaboration XIII, 2016b, A&A, 594, A13
Planck Collaboration XXI, 2016c, A&A, 594, A21
Prakash A. et al., 2016, ApJS, 224, 34
Price-Whelan A. M. et al., 2018, AJ, 156, 18
Raccanelli A., Bonaldi A., Negrello M., Matarrese S., Tormen G., de Zotti G., 2008, MNRAS, 386, 2161
Rácz G., Dobos L., Beck R., Szapudi I., Csabai I., 2017, MNRAS, 469, L1
Rassat A., Land K., Lahav O., Abdalla F. B., 2007, MNRAS, 377, 1085
Reid B. et al., 2016, MNRAS, 455, 1553
Riess A. G. et al., 1998, AJ, 116, 1009
Ross N. P., Shanks T., Cannon R. D., Wake D. A., Sharp R. G., Croom S. M., Peacock J. A., 2008, MNRAS, 387, 1323
Ross A. J. et al., 2012, MNRAS, 424, 564
Ross A. J. et al., 2017, MNRAS, 464, 1168
Sachs R. K., Wolfe A. M., 1967, ApJ, 147, 73
Sawangwit U., Shanks T., Cannon R. D., Croom S. M., Ross N. P., Wake D. A., 2010, MNRAS, 402, 2228
Sawangwit U., Shanks T., Abdalla F. B., Cannon R. D., Croom S. M., Edge A. C., Ross N. P., Wake D. A., 2011, MNRAS, 416, 3033
Schneider D. P. et al., 2007, AJ, 134, 102
Scranton R. et al., 2003, preprint (arXiv:astro-ph/0307335)
Shanks T. et al., 2015, MNRAS, 451, 4238
Taylor M. B., 2005, in Shopbell P., Britton M., Ebert R., eds, ASP Conf. Ser. Vol. 347, Astronomical Data Analysis Software and Systems XIV. Astron. Soc. Pac., San Francisco, p. 29
Vielva P., Martínez-González E., Tucci M., 2006, MNRAS, 365, 891

APPENDIX A: ATLAS/SDSS COLOUR COMPARISON

Fig. A1 shows a comparison of VST ATLAS Aperture 5 and SDSS model magnitude colours. Upon removing 3σ outliers (as indicated by the dashed lines in the plots), we find an rms scatter of 0.03, 0.04, and 0.13, with ATLAS-SDSS offsets of 0.01, −0.01, and 0.05 for $g-r$, $r-i$, and $i-z$ colours, respectively. Here, we impose magnitude limits of $g < 21.5$, $r < 19.5$, $i < 20.5$, and $z < 20.0$, corresponding to the range of magnitudes used in our LRG selection. In each case, we only impose the magnitude limits of the two bands used to obtain the colours and restrict the sample to galaxies based on the ATLAS morphological classification in those bands. Given the reasonably tight scatter and small systematic offsets, in this work we adopt a photometric selection criteria based on SDSS magnitudes, when defining our LRG samples.

APPENDIX B: LRG CONTAMINATION TESTS

Adopting a similar approach to Ross et al. (2017), we test for the impact of various sources of survey systematics including airmass, seeing, galactic dust extinction, and stellar contamination on our $\bar{z} = 0.35$, 0.55, and 0.68 LRG samples. In the top panel of Fig. B1, we show the four instances where systematic trends due to galactic extinction, seeing, and stellar contamination appear to be present in our LRG samples, finding no major systematic trends in the remaining cases. As shown in the bottom panel of Fig. B1, the inclusion of weights correcting for these observed systematics does not appear to have a significant impact on our ISW measurements.

Downloaded from https://academic.oup.com/mnras/article-abstract/493/4/4830/5766327 by University of Durham user on 20 March 2020

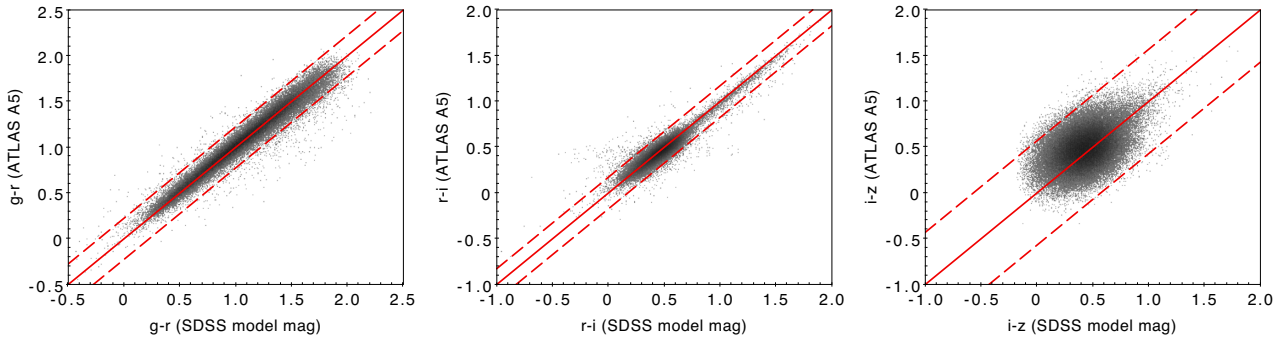

Figure A1. A comparison of the $g-r$, $r-i$, and $i-z$ colours based on VST ATLAS Aperture 5 and SDSS model magnitudes. Given the similarity between the colours, we use the SDSS cuts in our LRG sample selections, described in Section 2.2. Here, the dashed lines indicate the 3σ outliers.

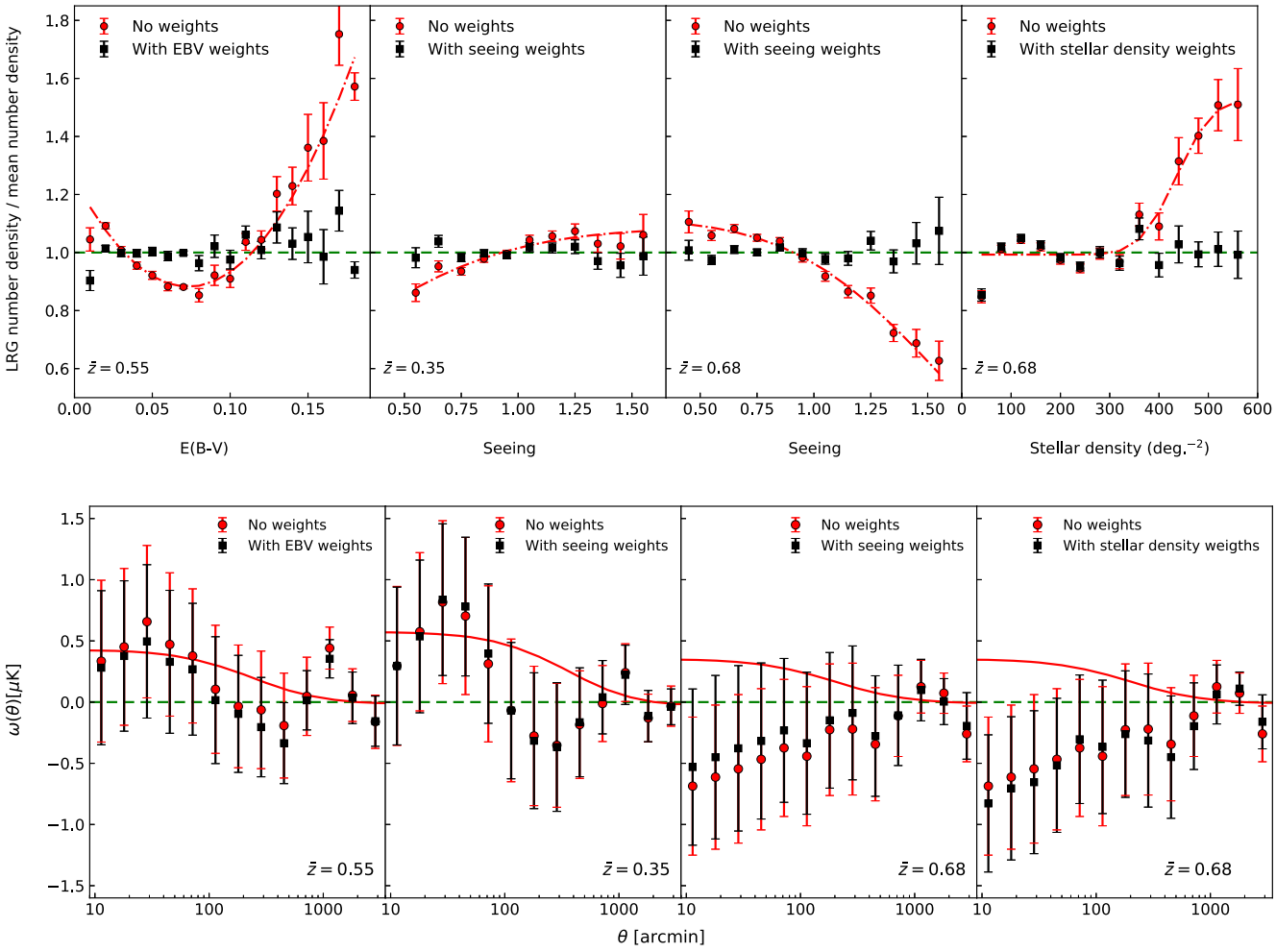

Figure B1. Top panel: Normalized projected LRG number density as a function of Galactic extinction (in $E(B-V)$), seeing (in r band for $\bar{z} = 0.35$ and i band for $\bar{z} = 0.68$), and projected stellar density (limited to $19.8 < i < 20.5$ corresponding to the magnitude limits of the $\bar{z} = 0.68$ LRG sample). Here, the dot–dashed curves are the best-fitting relationships used to define the weights correcting for the observed systematic trends. Bottom panel: The impact of including the $E(B-V)$, seeing, and stellar density weights from the top panel on our ISW measurements. In all cases, the inclusion of weights does not appear to have a significant impact on our ISW measurements.

This paper has been typeset from a TEX/LATEX file prepared by the author.

Downloaded from https://academic.oup.com/mnras/article-abstract/493/4/4830/5766327 by University of Durham user on 20 March 2020